Monitoring of Tectonic Deformation by Mining Satellite Image Time Series

Christophe Rigotti, Felicity Lodge, Nicolas Méger, Catherine Pothier, Romain Jolivet, Cécile Lasserre

Monitoring of Tectonic Deformation by Mining Satellite Image Time Series

Christophe Rigotti[1], Felicity Lodge[2], Nicolas Méger[2],
Catherine Pothier[3], Romain Jolivet[4] and Cécile Lasserre[5]

[1] Université de Lyon, CNRS, INRIA, INSA-Lyon, LIRIS laboratory (UMR 5205), Villeurbanne, France
christophe.rigotti@insa-lyon.fr
[2] Université de Savoie, Polytech Annecy-Chambéry, LISTIC laboratory, Annecy-le-Vieux, France
nicolas.meger,felicity.lodge@univ-savoie.fr
[3] Université de Lyon, INSA-Lyon, LGCIE laboratory, Villeurbanne, France
catherine.pothier@insa-lyon.fr
[4] Tectonics Observatory, California Institute of Technology, Pasadena, United States
rjolivet@caltech.edu
[5] Université Joseph Fourrier, CNRS, IsTerre Laboratory (UMR 5559), Grenoble, France
cecile.lasserre@ujf-grenoble.fr

Résumé

Cet article présente une nouvelle approche pour l'analyse de séries d'images satellite InSAR (Interferometric Synthetic Aperture Radar) et son application au monitoring de fluage le long d'une faille sismique active majeure. Les données InSAR permettent de mesurer les déformations du sol entre deux dates sur de grandes zones géographiques, mais la précision des mesures reste limitée par le bruit dû aux variations en temps et en espace des conditions atmosphériques. L'approche proposée combine des techniques d'analyse d'images satellite et des techniques de fouille de données. Elle permet de traiter des séries d'images satellite InSAR de façon non supervisée, même avec des conditions atmosphériques variables, et fournit aux experts des cartes décrivant les évolutions des déformations du sol. Des résultats expérimentaux sur une série d'images ENVISAT de la faille de Haiyuan (zone Nord-Est du plateau tibétain) sont présentés. Les cartes obtenues montrent un glissement asismique continu superficiel le long d'une portion de la faille, ce qui est consistant avec les modèles géophysiques actuels.

Mots-clefs

Télédétection, Déformation tectonique, Série temporelle d'images satellite, InSAR, Motif spatiotemporel

Abstract

In this paper, an original approach for analyzing Interferometric Synthetic Aperture Radar (InSAR) time series is presented and applied to the monitoring of creep along a major active fault. InSAR data are computed from satellite acquisitions and allow ground deformations occurring between different dates to be measured with high precision over large areas. However, measurement precision remains limited by the atmospheric noise, due to variations in space and time of atmospheric conditions. The proposed approach is designed to process InSAR data in an unsupervised way. It handles varying atmospheric conditions and provides end-users with spatiotemporal maps describing ground deformation evolutions. Experimental results on an ENVISAT InSAR time series covering the Haiyuan fault in the north-eastern boundary of the Tibetan plateau are presented. The maps obtained reveal continuous, aseismic shallow slip along a section of the fault, which is consistent with geophysical models. These results illustrate the potential of the proposed approach which combines advanced InSAR processings and data mining techniques.

Keywords

Remote sensing, Tectonic deformation, Satellite image time series, InSAR, Spatiotemporal pattern

1 Introduction

Satellite Image Time Series (SITS) are now widely available and represent huge amount of data that need to be analyzed to understand/monitor geophysical phenomena. A SITS is simply a series of images of the same area, but at different dates, obtained by optical or radar sensors. A very interesting kind of SITS are the time series obtained by Synthetic Aperture Radar Interferometry (InSAR) that depict ground deformations over large areas (tens of kilometers) with high precision of measurement of deformation amplitude (a few centimeters). In such an InSAR SITS, a pixel, at location (x, y) in an image, has a value that corre-

sponds to the deformation. The value indicates if the surface at this location (x, y) is moving toward the satellite or is moving away from the satellite. For the same location, the value of the pixel can be different over time and thus changes over the series.

The two main limitations of interferometry come from local changes of the nature of the surfaces, which reduce the coherence of measurements between images, and from variations in atmospheric conditions between the different acquisitions. The loss of coherence is easy to detect, while the atmospheric perturbations are difficult to discriminate from the displacement signal. The systemic uncertainty due to the contribution of the stratified atmosphere can be reduced by using Digital Elevation Models (DEM) and meteorological data, but random errors due to the turbulent atmosphere still degrade interferograms. In this paper, we compute the InSAR SITS using a dedicated tool (the NSBAS package [1]) that removes the contribution of the variations of the stratified atmosphere. Then, to overcome the problem of the presence of turbulent atmosphere, we extracted from this InSAR SITS the GFS-patterns (Grouped Frequent Sequential Patterns) of [2] (designed to find spatiotemporal regularities in SITS). Finally, we present how these patterns can be used to draw maps depicting ground deformations over space and time.

This paper is organized as follows. The next section briefly reviews methods for the analysis of SITS. The approach proposed here to find evolutions of ground deformations in SITS is presented in Section 3. Then, using data acquired by the ENVISAT satellite, experimental results on an InSAR time series covering the Haiyuan fault in the northeastern boundary of the Tibetan plateau are presented in Section 4.

2 Satellite image time series analysis

SITS can be processed in an unsupervised way at a higher level than the pixel one, after having identified objects or groups of pixels forming regions of interest. For example, in [3], textural, spatial and spectral features are extracted using stochastic models to further cluster data using appropriate representation spaces. Using the clusters that are obtained, spatiotemporal graphs are inferred and proposed to end-users. Several assumptions must be made: statistical image models such as Gibbs-Markov random fields are introduced, clusters are meant to follow Gaussian shapes and graphs are built taking into account additional spatial constraints. Spatiotemporal patterns can also be extracted from SITS at the image level by mining a sequence of signatures as proposed in [4]. In this case, self-organizing maps are used to extract signatures of each image. A SITS is then encoded as a sequence of image signatures. This sequence is further searched under temporal and frequency constraints to find serial episode-based rules [5] such as $A \Rightarrow B$ which can be read as *if signature A is observed once or more, then, sometime later, signature B is observed once or more*. This technique requires end-users to define the scale of the observed phenomena. This family of unsupervised approaches still needs, as input, assumptions about features/objects/regions that have to be identified and studied. This is not a trivial task since groups of pixels do not always form objects in a single image[1] (e.g., because of atmospheric perturbations, shading phenomena).

Per-pixel SITS analysis techniques have also gained attention as they do not require prior object identification. These are essentially clustering techniques. The feature vector associated with each pixel, and used to compare them, can contain aggregated values over time (e.g., average or min/max of the values associated to the pixel) as in [6], if the user has some insight about the kind of aggregates that are appropriate. The feature vector can also be the whole vector of values associated with the pixel over time, leading to a clustering which must be performed in a high dimensional space. Such a clustering can be difficult to interpret and requires careful parameter setting [7] as well as sophisticated distances such as the adaptation of the Levenshtein edit distance proposed in [8] to measure the distance between the sequences of values associated with pixels. These approaches perform per-pixel analysis without prior knowledge of the objects (or identified regions) to monitor. However, they require the incorporation of domain knowledge in the form of feature/aggregation/distance definitions, and they do not find overlapping areas or areas that refine other areas.

Other approaches based on change detection generate a single image in which changes are plotted, i.e., a change map. Change detection techniques generally require prior information about the type of changes that must be taken into account, and are targeted to a specific phenomenon. For example, some may want to look for abrupt changes such as floods, earthquakes or anthropic disasters (e.g., [9]), while others may be interested in gradual changes such as biomass accumulation (e.g., [10]).

3 Finding evolutions of ground deformations

For the preprocessing of raw satellite data, we use the NSBAS package [1] to handle atmospheric perturbations due to the stratified atmosphere, and to produce an InSAR SITS in which remaining noise is mostly due to the turbulent atmosphere. Then in order to avoid making assumptions about objects and value evolutions, and also to avoid the need for user supply domain knowledge, we make use of the GFS-patterns introduced in [2]. The GFS-patterns mining belongs to the family of per-pixel SITS analysis techniques, and offers several advantages: it does not required prior knowledge and can find spatiotemporal regularities in large and noisy datasets.

[1] This cannot be easily overcome, for instance, by averaging pixel values over consecutive images, since the aspect of an object is likely to change from one image to the next.

3.1 Pattern definition

GFS-patterns denote evolutions of discrete states at the pixel level. First, the SITS needs to be discretized, and each pixel value is encoded by a label representing a discrete pixel state. The discretization intervals are determined by using for instance equal interval bucketing or equal frequency bucketing (percentiles). A pixel evolution is then described using an sequential pattern, denoted $A_1 \rightarrow A_2 \rightarrow \ldots \rightarrow A_n$, where $A_1, A_2, \ldots, A_n$ are symbols representing discrete pixel states at n different dates which are not necessarily consecutive (when clear from the context, the arrow could be omitted). A pixel at location (x, y) is said to satisfy to an evolution $\alpha = A_1 \rightarrow A_2 \rightarrow \ldots \rightarrow A_n$ if at this location we encounter in the SITS these discrete values in the same order, but not necessarily in strictly consecutive images.

The pixels satisfying to α are said to *be covered* by α and the set of these pixels is denoted $cov(\alpha)$. The size $|cov(\alpha)|$ is called the *support* of α. The pixels covered by a pattern are also required to exceed a minimum connectivity threshold κ. The connectivity measure used is called the *average connectivity*. It gives, for the pixels satisfying to α, the average number of pixels in their neighborhood also satisfying to α. The 8 nearest neighbors (8-NN) are taken into consideration. Let us consider a *local connectivity function* $LC((x, y), \alpha)$ that returns, for a pixel (x, y), the number of neighbors covered by α. The average connectivity of α is then defined as $AC(\alpha) = \frac{\sum_{(x,y) \in cov(\alpha)} LC((x,y),\alpha)}{|cov(\alpha)|}$. For two given thresholds σ and κ, an evolution α is called an *GFS pattern* if $|cov(\alpha)| \geq \sigma$ and if $AC(\alpha) \geq \kappa$ (for a more detailed presentation, the reader is referred to [2]). In a SITS, a GFS-pattern is an evolution that covered a sufficiently large surface (at least σ pixels) formed by pixels that tend to be grouped in space.

It is worth noting that:

- to satisfied to a pattern, the dates of occurrences of the states are not required to be strictly consecutive;
- sequences of states for pixels sharing a same pattern do not need to be synchronized in time;
- no time constraint is set;
- the shape of the observed phenomena is not set beforehand;
- a wide range of scales can be taken into account (all surfaces greater or equal to σ pixels).

In addition, the more a pattern contains pixel states, the more the surface constraint and the connectivity constraint ensure that it relates to a less-random phenomenon. Indeed, long patterns that could be built from noisy acquisitions are not likely to be satisfied over a large connected surface as random phenomena such as noise or atmospheric turbulences are dispersed over time and space.

3.2 Pattern usage

To give a general view of the spatiotemporal evolutions of ground deformations, we first cluster the GFS-patterns according to the sets of pixels they cover. If two patterns cover similar sets of pixels they are considered to be close to each other in the clustering space. More precisely, for a pattern α and a pattern β, the distance d between them is expressed as follows: $d(\alpha, \beta) = 1 - \frac{|cov(\alpha) \cap cov(\beta)|}{|cov(\alpha) \cup cov(\beta)|}$. We use a bottom-up hierarchical algorithm with a complete link distance (see [11]) to perform the clustering. A color is then associated to each cluster, and the clusters are visualized on a map of the same size as the images of the SITS. In this map, the black color is assigned to pixels that are not covered by any GSF-pattern. The white color is used for pixels covered by GFS-patterns of different clusters. Each remaining pixel is covered by one or more patterns all belonging to the same cluster, and then is associated to the color of this cluster.

Then, to provide a more detailed view of the spatiotemporal evolutions of the ground deformations, we build one map per pattern as follows. For a GFS-pattern α, we draw a map (again of the same size as the images of the SITS) where pixels that are not covered by α are set to the black color. For the other pixels, we use in this map a color scale to represent the temporal dimension, and the color of a pixel at location (x, y) is set to a value that reflects the date at which the evolution α has been found at this location (more precisely the earliest ending date of occurrence of α at location (x, y)). Such a map gives at a glance the spatiotemporal localization of a ground deformation evolution over the whole SITS, and as reported in Section 4, it captures useful information to monitor seismic faults.

4 Experiments on Haiyuan ENVISAT InSAR time series

Experiments have been run on an ENVISAT InSAR time series covering the Haiyuan fault at the north-eastern boundary of the Tibetan plateau. This fault is at the origin of two major earthquakes (magnitude $M \sim 8$) in the early 20th century and a seismic gap with a high seismic hazard has been identified in between both rupture areas [12].

4.1 Data preparation

The raw data are acquisitions (ENVISAT ascending track) made over the 2003-2009 period. The InSAR SITS has been prepared using the NSBAS processing chain [1], based on the ROI_PAC software [13]. Snapshots for three acquisition dates are shown in Figure 1 (North at the top and West on the right).

4.2 Deformation evolution mining

We obtained a SITS of 24 cumulated displacement images (701×701 pixels) covering an area of about 50 km $\times$ 50 km. In these images, positive (resp. negative) values correspond to motion away from (resp. towards) the satellite,

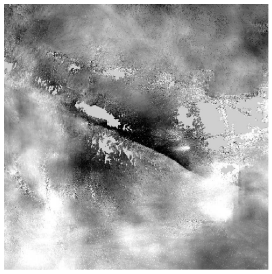

(a) 2004/01/15 - 2006/09/2

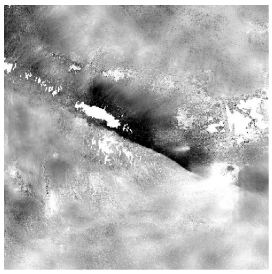

(b) 2004/01/15 - 2008/02/28

(c) 2004/01/15 - 2009/08/06

Figure 1: Snapshots of displacement at 3 acquisition dates, in satellite geometry. A white (reps. black) color denotes a motion away from (reps. towards) the satellite.

along the line of sight. It is important to notice that because of the geometric configuration, these displacements contain both vertical and lateral components of the ground motion. The whole SITS was discretized using 3 symbols ('1', '2' and '3') by using the 33rd and the 66th centiles. Symbol '1' represents large negative values, symbol '2' corresponds to low negative values and symbol '3' denotes positive values. The GFS-pattern extraction was run on a standard laptop (Intel Core i5 @ 2.5 GHz, 8 GB of RAM, Linux 3.1.0 kernel) by setting the minimum surface threshold σ to 100000 pixels (i.e., about 20% of the surface of an image) and the average connectivity threshold κ to 6. This minimum surface setting ensures that wide zones/large surfaces are considered. The minimum connectivity is set to a high value so as to discard isolated deformations. Within less than 35 minutes, 3398 GFS-patterns were extracted along with their respective surfaces and average connectivity, using the technique presented in [2]. In order to focus on the most specific patterns and to discard atmospheric perturbations (see Section 3.1), the longest GFS-patterns were selected, which amounts to a total of 20 patterns: 19 patterns with 10 symbols and one pattern having 11 symbols (the other patterns have at most 9 symbols).

GFS-pattern clustering. First, the 20 patterns were clustered as presented in Section 3.2. The best clustering result was obtained for two clusters. The composition of these clusters is given Table 1. It is important to notice that the distance used for the clustering is not based directly on the symbols appearing in the patterns, but that two patterns are put in the same cluster if they tend to cover the same pixels. Table 1 shows that the patterns covering the same areas are patterns having similar syntactic forms, and advocates for the coherence of the spatiotemporal information retrieved by mean of the patterns.

Table 1: Composition of the two clusters

Cluster #1	Cluster #2
1,1,1,1,1,1,1,1,1,1	2,3,3,3,3,3,3,2,3,3
1,1,1,1,1,1,1,1,2,1	2,3,3,3,3,3,3,3,2,3
1,1,1,1,1,1,1,2,1,1	2,3,3,3,3,3,3,3,3,3
1,1,1,1,1,1,2,1,1,1	3,2,3,3,3,3,3,3,2,3
1,1,1,1,1,2,1,1,1,1	3,2,3,3,3,3,3,3,3,3
1,1,1,1,2,1,1,1,1,1	3,3,3,3,2,3,3,3,3,3
1,1,1,1,2,2,1,1,1,1	3,3,3,3,3,2,3,3,3,3
2,1,1,1,1,1,1,1,1,1	3,3,3,3,3,3,3,2,3,3
	3,3,3,3,3,3,3,3,2,3
	3,3,3,3,3,3,3,3,3,2
	3,3,3,3,3,3,3,3,3,3,3
	3,3,3,3,3,3,3,3,3,3

The two clusters were then visualized on an image (see Section 3.2) using yellow and red respectively for cluster #1 and cluster #2. The resulting image is given Figure 2a.

(a) Localization of the two clusters.

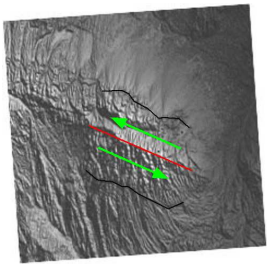

(b) Shaded relief showing main active fault in red, minor ones in black and known horizontal motions shown by green arrows.

Figure 2: Clustering results, study site topography and known horizontal motions on both sides of the fault.

The known faults and horizontal motions in the area are depicted Figure 2b. The main fault (in red) delimits two blocks moving in opposite directions, as the result of shallow, left-lateral creep along a 30 km long segment of the fault: a northwestward lateral movement north of the fault, and a southeastward movement south of the fault. The main fault corresponds to the diagonal border between the yellow and the red clusters at the center of the image Figure 2a. During the acquisition, the satellite was located on the left of the image. All patterns of the yellow cluster are essentially made of symbol 1 (meaning that the area moves closer to the satellite). The part of the yellow cluster located immediately north of the fault thus corresponds to a motion which is coherent with the tectonic creep motion to the northwest Figure 2b. The same holds for the red cluster, made of patterns containing mainly the symbol 3 (motion away from the satellite), and for which the part immediately south of the main diagonal fault corresponds

to the motion towards the southeast Figure 2b. The other parts of the two clusters depict other large areas in motion, in particular a large yellow area along the left and bottom border of the image, and a large red area along nearly all the top border. These motions might be due to seasonal water table fluctuations, in particular in areas of prominent alluvial fans, or (more likely) to other vertical tectonic motions (uplift south of the fault and subsidence north of it) not yet modeled by the experts.

GFS-pattern spatiotemporal visualization. While the clustering of the patterns and the visualization of the clusters depict global motions, the visualization of each pattern separately reveals more detailed phenomena. To this aim, each pattern was visualized as an image (see Section 3.2). The colors used range from red (early dates in the series) to violet (late dates in the series) according to the color scale given in Figure 3d. The results obtained for two different GFS-patterns, "1,1,1,1,1,1,1,1,2,1" and "3,3,3,3,3,3,3,3,3,2", are shown on figures 3a and 3b respectively. These patterns are associated with one of each cluster presented in Figure 2a, and, as the two respective clusters they belong to, they capture, in the central part of the image, the motions toward the northwest and southeast for the areas close to the main fault. Furthermore, the color map used to encode the ending date of the occurrences of these patterns reveals additional spatiotemporal information. On both images along the main fault, two smooth gradients of ending dates can be observed (white arrows), from light blue to violet. These variations may indicate a creep migration and/or creep rate changes along strike, at shallow depth or at deeper levels.

Some patterns can also reveal more specific behavior. This is illustrated Figure 3c. The area in the white circle could be expected to move horizontally towards the left, when we refer to the motions along the main fault in Figure 2b. On the contrary, the pattern "3,2,3,3,3,3,3,3,3,3" of Figure 3c indicates that this area is moving away from the satellite (symbol 3). This is because the fault is not a straight line, but has some geometrical irregularities. The area in the white circle corresponds here to a major left step-over along the fault, marked by a pull-apart basin that subsides.

All the patterns presented in the previous figures have been extracted with a minimum surface threshold σ of 100000 pixels (about 20% of the surface of an image). Of course, patterns can be extracted for smaller thresholds to attempt to focus on more specific areas. For instance the pattern "3,3,3,3,3,1,1,3,2,3,3,2,1" of Figure 3e has been obtained with σ = 20000 pixels (about 4% of the surface of an image). Its covered area corresponds mostly to an area containing alluvial fans located in the white circle Figure 3f. The sequence of symbols in the pattern indicates alternate motions (toward and away from the satellite) that could be due to seasonal water table fluctuations.

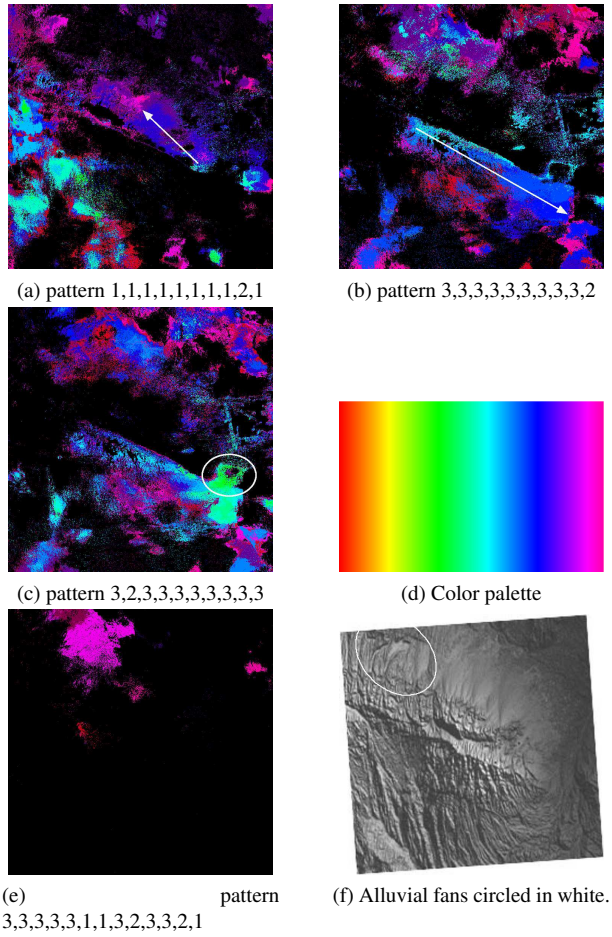

(a) pattern 1,1,1,1,1,1,1,1,2,1 (b) pattern 3,3,3,3,3,3,3,3,3,2 (c) pattern 3,2,3,3,3,3,3,3,3,3 (d) Color palette (e) pattern 3,3,3,3,3,1,1,3,2,3,3,2,1 (f) Alluvial fans circled in white.

Figure 3: Color palette and spatiotemporal localization of patterns.

5 Conclusions

The results presented in this paper illustrate the potential of a combined use of advanced InSAR multitemporal processing for deriving displacement time series and of data mining techniques to analyze SITS. We shown that such an approach is effective to find in an unsupervised way spatiotemporal features corresponding to ground deformations, even in the presence of atmospheric perturbations leading to systematic uncertainty (atmosphere stratification) and random uncertainty (atmosphere turbulence). Using GFS-patterns, known (tectonic) and unknown (likely hydrological or anthropic) phenomena have been indeed found without introducing any refined knowledge about them. More precisely, an initial clustering of the GFS-patterns was shown to be relevant to highlight the main tectonic phenomena and an increased knowledge on the geophysical behavior has been obtained from GFS-pattern spatiotemporal visualizations.

Acknowledgments

This work was supported by the French Research Agency (ANR) through the FOSTER project (ANR-2010-COSI-

012-04, http://foster.univ-nc.nc). The authors wish to thank the European Space Agency (ESA) for the ENVISAT SAR data (Dragon project ID5305) over the Haiyuan fault.

References

[1] M.-P. Doin, S. Guillaso, R. Jolivet, C. Lasserre, F. Lodge, G. Ducret, and R. Grandin, "Presentation of the small-baseline NSBAS processing chain on a case example: the etna deformation monitoring from 2003 to 2010 using ENVISAT data," in *Proc. of the European Space Agency Symposium "Fringe"*, Frascati, Italy, 2011, pp. 3434–3437.

[2] A. Julea, N. Méger, P. Bolon, C. Rigotti, , M.-P. Doin, C. Lasserre, E. Trouvé, and V. Lăzărescu, "Unsupervised spatiotemporal mining of satellite image time series using grouped frequent sequential patterns," *IEEE Transactions on Geoscience and Remote Sensing*, vol. 49, no. 4, pp. 1417–1430, 2011.

[3] P. Héas and M. Datcu, "Modeling trajectory of dynamic clusters in image time-series for spatio-temporal reasoning," *Geoscience and Remote Sensing, IEEE Transactions on*, vol. 43, no. 7, pp. 1635–1647, 2005.

[4] R. Honda and O. Konishi, "Temporal rule discovery for time-series satellite images and integration with RDB," in *PKDD '01: Proceedings of the 5th European Conference on Principles of Data Mining and Knowledge Discovery*. London, UK: Springer-Verlag, 2001, pp. 204–215.

[5] H. Mannila, H. Toivonen, and A. I. Verkamo, "Discovery of frequent episodes in event sequences," *Data Mining and Knowledge Discovery*, vol. 1, no. 3, pp. 259–289, 1997.

[6] E. Nezry, G. Genovese, G. Solaas, and S. Rémondière, "ERS - Based early estimation of crop areas in Europe during winter 1994-95," in *ERS Application, Proceedings of the Second International Workshop held 6-8 December 1995 in London*, ser. ESA Special Publication, G. T.-D., Ed., vol. 383, 1996, p. 13.

[7] L. Gallucio, O. Michel, and P. Comon, "Unsupervised clustering on multi-components datasets: Applications on images and astrophysics data," in *16th European Signal Processing Conference EUSIPCO-2008*, Lausanne, Switzerland, august 2008, pp. 25–29.

[8] A. Ketterlin and P. Gançarski, "Sequence similarity and multi-date image segmentation," in *4th Intl Workshop on the Analysis of Multi-temporal Remote Sensing Images*, Leuven, Belgique, july 2007. [Online]. Available: http://lsiit.u-strasbg.fr/Publications/2007/KG07

[9] J. Inglada, J.-C. Favard, H. Yesou, S. Clandillon, and C. Bestault, "Lava flow mapping during the Nyiragongo January, 2002 eruption over the city of Goma (D.R. Congo) in the frame of the international charter space and major disasters," in *IGARSS*, vol. 3, july 2003, pp. 1540–1542.

[10] A. Vina, Echavarria, F. R., and Rundquist, "Satellite change detection analysis of deforestation rates and patterns along the colombia-ecuador border," *AMBIO: A Journal of the Human Environment*, vol. 33, pp. 118–125, 2004.

[11] P.-N. Tan, M. Steinbach, and V. Kumar, *Introduction to Data Mining, (First Edition)*. Boston, MA, USA: Addison-Wesley Longman Publishing Co., Inc., 2005.

[12] Y. Gaudemer, P. Tapponnier, B. Meyer, G. Peltzer, G. Shunmin, C. Zhitai, D. Huagung, and I. Cifuentes, "Partitioning of crustal slip between linked, active faults in the eastern qilian shan, and evidence for a major seismic gap, the 'tianzhu gap', on the western haiyuan fault, gansu (china)," *Geophysical Journal International*, vol. 120, no. 3, pp. 599–645, 1995.

[13] P. A. Rosen, S. Henley, G. Peltzer, and M. Simons, "Updated repeat orbit interferometry package released," *Eos Trans. American Geophysical Union*, vol. 85, no. 5, 2004.